HOKKAIDO UNIVERSITY

Title	Plasma flow modeling for Huels-type arc heater with turbulent diffusion
Author(s)	Takahashi, Yusuke; Esser, Burkard; Steffens, Lars et al.
Citation	Physics of Plasmas, 24(12), 123509 https://doi.org/10.1063/1.5008909
Issue Date	2017-12
Doc URL	https://hdl.handle.net/2115/67926
Rights	Copyright 2017 American Institute of Physics. This article may be downloaded for personal use only. Any other use requires prior permission of the author and AIP Publishing. The following article appeared in Physics of Plasmas 24, 123509 (2017) and may be found at http://aip.scitation.org/doi/abs/10.1063/1.5008909
Type	journal article
File Information	aper_l2k_modeling.pdf

Hokkaido University Collection of Scholarly and Academic Papers : HUSCAP

Plasma Flow Modeling for Huels-Type Arc Heater with Turbulent Diffusion

Yusuke Takahashi[1],
Hokkaido University, Kita 13 Nishi 8, Kita-ku, Sapporo, Hokkaido 060-8628, Japan
and
Burkard Esser[2], Lars Steffens[3], and Ali Gülhan[4]
German Aerospace Center (DLR), Linder Höhe, Cologne 51147, Germany

Abstract

In this study, we developed an analytical model for the flow field in the Huels-type arc-heated wind tunnel (L2K) of the German Aerospace Center. This flow-field model can be used to accurately reproduce the discharge behavior in the heating section and expansion in the nozzle section of L2K. It includes the radiation transport and turbulent flow, as well as thermochemical nonequilibrium models, which are tightly coupled with electric field calculations. In addition, we considered the turbulent diffusion model for the mass conservation of the species and performed numerical simulations for several cases with and without the turbulent diffusion model. Computations were used to obtain the general characteristics of an arc-heated flow containing an arc discharge and supersonic expansion. We verified that radiation and turbulence play important roles in the transfer of heat from the high-temperature core flow to the outer cold gas in the heating section of L2K. In addition, we performed parametric studies that involved varying the degree of turbulent diffusion. The results showed that turbulent diffusion has a large influence on the formation of the arc discharge in the heating section and on the enthalpy distribution at the nozzle exit.

Nomenclature

B	=	blackbody function, W/m^3
C	=	mass fraction
C_p	=	specific heat at constant pressure, J/(kg·K)
D	=	effective diffusion coefficient, m^2/s
e	=	electric charge, C, or energy per unit mass, J/kg
E	=	internal energy, J/m^3, or electric field, V/m
h	=	enthalpy, J/kg
H_{ave}	=	mass-averaged enthalpy, J/kg
Δh^0	=	enthalpy of formation, J/kg
I	=	current, A, or radiation intensity, W/m^3
j	=	current density, A/m^2
k	=	Boltzmann constant, J/K, or turbulent kinetic energy, J/kg,

[1]Assistant Professor, Faculty of Engineering; ytakahashi@eng.hokudai.ac.jp, Visiting Researcher, Supersonic and Hypersonic Technologies Department of the Institute of Aerodynamics and Flow Technology, German Aerospace Center (DLR).

[2]Research Scientist, Supersonic and Hypersonic Technologies Department of the Institute of Aerodynamics and Flow Technology, German Aerospace Center (DLR).

[3]Research Scientist, Supersonic and Hypersonic Technologies Department of the Institute of Aerodynamics and Flow Technology, German Aerospace Center (DLR).

[4]Head of Department, Supersonic and Hypersonic Technologies Department of the Institute of Aerodynamics and Flow Technology, German Aerospace Center (DLR).

	=	or reaction-rate coefficient, $m^3/(mole \cdot s)$
K^{eq}	=	equilibrium constant
m	=	mass, kg
M	=	Mach number, or molecular species
n	=	number density, $1/m^3$
nm	=	number of molecular species
ns	=	number of species
p	=	pressure, N/m^2
Pr_t	=	turbulent Prandtl number
q	=	heat flux, W/m^2
R	=	gas constant, $J/(kg \cdot K)$, or, radius, m
s	=	species
S_{int}	=	internal energy-exchange rate, W/m^3
S_{joule}	=	Joule-heating rate, W/m^3
S_{rad}	=	radiation source tern, W/m^3
Sc_t	=	turbulent Schmidt number
t	=	time, s
T	=	temperature, K
u	=	velocity, m/s
V	=	voltage, V
$\dot{w}$	=	mass-production rate, $kg/(m^3 \cdot s)$
x	=	coordinate, m
X	=	mole fraction
γ	=	specific heat ratio
δ_{ij}	=	Kronecker delta
θ	=	angle
Θ	=	characteristic temperature, K
κ	=	absorption coefficient, 1/m
λ	=	thermal conductivity, $W/(K \cdot m)$, or wavelength, m
μ	=	viscosity, $N \cdot s/m^2$
ρ	=	density, kg/m^3
σ	=	electrical conductivity, S/m
ϕ	=	electric potential, V
ω	=	relaxation parameter
Ω	=	solid angle

Subscripts

b	=	backward
ele	=	electron
f	=	forward
int	=	internal
joule	=	Joule heating
rad	=	radiation
rot	=	rotation
s	=	species
t	=	turbulent
trs	=	translation
vib	=	vibration

λ = wavelength

Superscripts

a = ambipolar
con = convection
n = time step
rad = radiation

1 Introduction

Arc-heated wind tunnels are widely used to reproduce a high-enthalpy flow, e.g., planetary entry environments, in ground-based facilities. Such ground-test facilities are primarily utilized in aerospace applications. In general, the arc heater of an arc-heated wind tunnel comprises mainly a constrictor (heating section) and nozzle (expansion section). The flow field in an arc heater is very complicated because of the Joule heating process, which is caused by the arc discharge in the constrictor, and strong thermochemical nonequilibrium, which is derived from supersonic expansion in the nozzle. Consequently, it is difficult to simultaneously measure all the properties of the arc-heated flow with high accuracy. However, obtaining the arc-heated flow properties such as the enthalpy, temperature, velocity, and species concentration is important for good-quality testing using an arc-heated wind tunnel.

To date, based on the efforts of many research groups, the Pitot pressure, heat flux, and mass-averaged enthalpy of arc-heated flows have been experimentally obtained. In addition, non-intrusive diagnostic approaches, e.g., spectroscopic analysis of the molecular band emission [1] and laser-induced fluorescence (LIF) [2–4], have been used for the arc-heated flow in a test chamber. The emission spectra of the arc column and heat flux for the constrictor have been measured to understand the heating behavior [5–7]. In addition, these have revealed the distributions of the translational temperature, flow velocity, and number density.

With the recent development of high-performance computers, numerical simulations have become effective tools for investigating the mechanisms of complex flow fields in detail. Several studies have investigated arc-heated flow properties using numerical analysis methods [8–12]. To achieve accurate predictions, it is important to construct a detailed model of the heating process in the constrictor and the expansion phenomena in the nozzle. For the heating process, it is desirable to couple the electric-field calculation with flow-field simulations, because the arc discharge significantly affects the formation of the arc-heated flow field. Because the expansion flow in the nozzle is excited both rotationally and vibrationally, it is necessary to separate the rotational and vibrational temperatures from the translational temperature. Abe et al. [8] and Takahashi et al. [13, 14] reported that the arc-heated flows in the Kyushu University wind tunnel (KUWT), which uses a constrictor-type 20 kW arc heater, are in strong thermochemical nonequilibrium. Moreover, their studies suggested that turbulence plays only a minor role in the 20 kW KUWT, because it is a small-scale facility. However, in relatively large arc-heating facilities, e.g., the Japan Aerospace Exploration Agency's (JAXA's) 750 kW segmented-type arc heater (JXWT) [15] and National Aeronautics and Space Administration's (NASA) 20 MW aerodynamic heating facility (AHF) [16], it was reported by Takahashi et al. [17] that both the turbulence and radiation are important for the heat transfer from the high-temperature gas (i.e., arc column) to the surrounding cold gas. Plasma flow simulations performed by Katsurayama et al. [18] and Yu et al. [19] indi-

cated that a higher-accuracy transport property model is effective at accurately predicting the discharge formation. Sahai et al. [20] carried out an unsteady three-dimensional (3D) simulation of the arc-heating flow in NASA's 20 MW AHF, and the dynamic process of the discharge attachment on electrodes was captured by the simulation. These recent efforts involving numerical studies mainly focused on constrictor-type and segmented-type arc-heated wind tunnels, whereas there are currently relatively few studies on the Huels-type arc heater.

In general, the electrical energy from the arc discharge is first input into thermal energy of test gas in the arc heater, and then rapidly transferred to chemical energy. Thus, the chemical component of the flow enthalpy is dominant in the total enthalpy, which includes thermal, kinetic, and pressure components. Because the turbulent diffusion of mass species strongly affects the chemical energy, it can be the key issue when modeling the turbulent diffusion to predict the arc-heated flow.

L2K [21] in the German Aerospace Center (DLR; Deutsches Zentrum für Luft- und Raumfahrt) is one of the largest Huels-type arc-heated wind tunnels in existence, and its maximum rated electrical power is 1.4 MW. Various flow properties have been measured using intrusive and non-intrusive techniques, and many operations have been performed, including performance tests of thermal protection systems and reduction tests of radio-frequency blackout [22]. However, there are some uncertainties regarding the discharge structure in the heating section and thermochemical nonequilibrium behavior in the expansion section. To acquire good-quality data, it is important to investigate the arc discharge behavior in the constrictor and the expansion process in the nozzle, as well as the turbulent flow behavior. Thus, the goal of this study was to develop and validate a numerical analysis model that considered the turbulent diffusion for a large-scale Huels-type arc heater. In addition, performing diagnostics on the arc-heated flow was within the scope of the study.

2 L2K Facility

L2K is one of the test legs of the Lichtbogenbeheizte Anlagen Köln (LBK) arc-heating facility [21] in DLR, whose second test leg, L3K, is a segmented-type arc-heated wind tunnel. These two facilities have individual test chambers, diffusers, and heat exchangers. Moreover, these facilities are connected to a common vacuum pumping system and nitric oxide absorption facility.

L2K, which is one of the Huels-type arc heaters, consists mainly of cathode and anode hollow tubes, an inlet section, a reservoir section, a throat section, and a nozzle section. The configuration of L2K is illustrated in Fig. 1. Hollow electrodes face each other. The test gas is injected from the inlet between the electrode tubes. Throats with diameters of 14, 20, 25, and 29 mm are available. Nozzles with diameters of 100, 200, and 300 mm, with a half angle of 12°, are used to generate a plasma flow with a Mach number of 4–8 in the test chamber. The gas is supplied at mass flow rates between 5 and 125 g/s. To stabilize the arc column by inputting the magnetic field, the spin coils are located external to both electrodes. The plasma flow in the electrode tubes is forced in the circumferential direction by the Lorentz force that is generated by the magnetic field and motion of the charged species. The averaged enthalpy at the nozzle exit reaches approximately 10 MJ/kg for an operating condition with a mass flow rate of 50 g/s and reservoir pressure of 1.5 MPa in the heating section. In addition, higher enthalpies are achievable at low mass flow rates, and the maximum operation duration is approximately 7200 s.

The operating parameters used in the investigation are listed in Table 1. The operat-

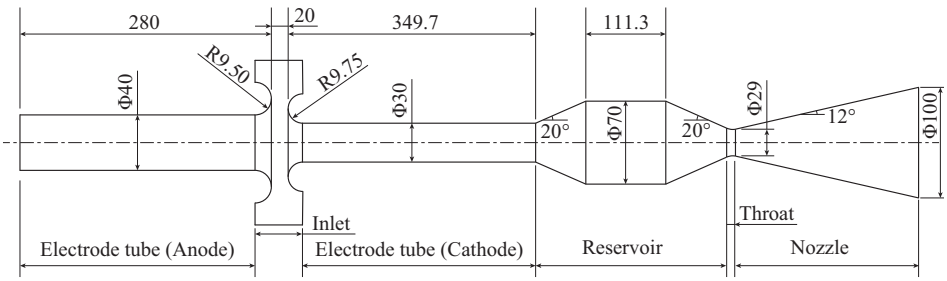

Figure 1: L2K configuration (all dimensions are in millimeters).

ing condition was applied in the European project Advanced Ablation Characterization and Modelling (ABLAMOD) [23] to generate validation data for ablation models. The measured arc voltage and reservoir pressure were approximately 720 V and 1×10^5 Pa under this operating condition, respectively. The flow properties were nearly homogeneous in the reservoir because of the strong mixture. The nozzle was set up with a throat of 29 mm and an exit diameter of 100 mm.

Table 1: Operating parameters.

Test gas	Air
Mass flow rate, kg/s	36×10^{-3}
Total temperature of gas, K	300
Input current, A	750

3 Mathematical Models

This section describes the governing equations and models used in the present numerical simulation approach.

3.1 Assumptions

In this paper, the following assumptions are made: (1) The flow is turbulent, steady, continuum, and axisymmetric without swirl. (2) The test gas is air. (3) The flow field is in thermochemical nonequilibrium, and the temperature is separated into translational, rotational, vibrational, and electron temperatures. (4) Because the arc current is too small to induce an effective magnetic field, the Lorentz force, Hall current, and ion slip by the induction can be neglected. (5) Radiation is considered.

3.2 Governing Equations

The flow field is described using the Navier-Stokes (N-S) equations extended to a thermochemically nonequilibrium flow and an equation of state. The N-S equations consist of the total mass, momentum, total energy, species mass, rotation energy, vibration energy, and

electron energy conservations, which are expressed as follows:

$$\frac{\partial \rho}{\partial t} + \frac{\partial}{\partial x_j}\left(\rho u_j\right) = 0, \tag{1}$$

$$\frac{\partial(\rho u_j)}{\partial t} + \frac{\partial}{\partial x_j}\left(\rho u_i u_j + \delta_{ij} p\right) = \frac{\partial}{\partial x_j}\left[\mu\left(\frac{\partial u_i}{\partial x_j} + \frac{\partial u_j}{\partial x_i} - \frac{2}{3}\frac{\partial u_k}{\partial x_k}\delta_{ij}\right)\right], \tag{2}$$

$$\begin{aligned}\frac{\partial E}{\partial t} + \frac{\partial}{\partial x_j}\left[\left(E+p\right)u_j\right] &= \frac{\partial}{\partial x_j}\left(\lambda_{\mathrm{trs}}\frac{\partial T_{\mathrm{trs}}}{\partial x_j} + \lambda_{\mathrm{rot}}\frac{\partial T_{\mathrm{rot}}}{\partial x_j} + \lambda_{\mathrm{vib}}\frac{\partial T_{\mathrm{vib}}}{\partial x_j} + \lambda_{\mathrm{ele}}\frac{\partial T_{\mathrm{ele}}}{\partial x_j}\right) \\ &+ \frac{\partial}{\partial x_j}\left(\rho\sum_{s=1}^{ns} h_s D_s \frac{\partial X_s}{\partial x_j}\right) + \frac{\partial}{\partial x_j}\left[u_j \mu\left(\frac{\partial u_i}{\partial x_j} + \frac{\partial u_j}{\partial x_i} - \frac{2}{3}\frac{\partial u_k}{\partial x_k}\delta_{ij}\right)\right] + S_{\mathrm{rad}} + S_{\mathrm{joule}},\end{aligned} \tag{3}$$

$$\frac{\partial \rho_s}{\partial t} + \frac{\partial}{\partial x_j}\left(\rho_s u_j\right) = \frac{\partial}{\partial x_j}\left(\rho D_s \frac{\partial X_s}{\partial x_j}\right) + \dot{w}_s, \tag{4}$$

$$\frac{\partial E_{\mathrm{rot}}}{\partial t} + \frac{\partial}{\partial x_j}\left(E_{\mathrm{rot}} u_j\right) = \frac{\partial}{\partial x_j}\left(\lambda_{\mathrm{rot}}\frac{\partial T_{\mathrm{rot}}}{\partial x_j}\right) + \frac{\partial}{\partial x_j}\left(\rho\sum_{s=M}^{nm} h_{\mathrm{rot},s} D_s \frac{\partial X_s}{\partial x_j}\right) + S_{\mathrm{int,rot}}, \tag{5}$$

$$\frac{\partial E_{\mathrm{vib}}}{\partial t} + \frac{\partial}{\partial x_j}\left(E_{\mathrm{vib}} u_j\right) = \frac{\partial}{\partial x_j}\left(\lambda_{\mathrm{vib}}\frac{\partial T_{\mathrm{vib}}}{\partial x_j}\right) + \frac{\partial}{\partial x_j}\left(\rho\sum_{s=M}^{nm} h_{\mathrm{vib},s} D_s \frac{\partial X_s}{\partial x_j}\right) + S_{\mathrm{int,vib}}, \tag{6}$$

$$\frac{\partial E_{\mathrm{ele}}}{\partial t} + \frac{\partial}{\partial x_j}\left[\left(E_{\mathrm{ele}} + p_{\mathrm{ele}}\right)u_j\right] = \frac{\partial}{\partial x_j}\left(\lambda_{\mathrm{ele}}\frac{\partial T_{\mathrm{ele}}}{\partial x_j}\right) + \frac{\partial}{\partial x_j}\left(\rho h_{\mathrm{ele}} D_{\mathrm{ele}} \frac{\partial X_{\mathrm{ele}}}{\partial x_j}\right) + S_{\mathrm{int,ele}} + S_{\mathrm{rad}} + S_{\mathrm{joule}}. \tag{7}$$

Because the flow field is assumed to be axisymmetric without swirl, no momentum equation was considered in the circumferential direction. Thus, the Lorentz force derived by the spin coil, which works on the momentum in this direction, is neglected in the present model. The total energy and electron-energy equations include a Joule-heating rate term that is related to the flow field and electric field. In addition, both equations are related to the radiation calculation using the radiation term. The internal energy conservation sources are coupled with each other through the energy exchange rate terms S_{int}.

The equation of state is given by

$$p = \sum_{s\neq \mathrm{ele}}^{ns} \rho_s R_s T_{\mathrm{trs}} + \rho_{\mathrm{ele}} R_{\mathrm{ele}} T_{\mathrm{ele}}. \tag{8}$$

The total energy, E, including the translational, rotational, and vibration internal energies,

is given by

$$E = E_{\mathrm{trs}} + E_{\mathrm{rot}} + E_{\mathrm{vib}} + E_{\mathrm{ele}} + \sum_{s}^{ns} \rho_s \Delta h_s^0 + \frac{1}{2}\rho u_j u_j, \tag{9}$$

$$E_{\mathrm{trs}} = \sum_{s\neq \mathrm{ele}}^{ns} \frac{3}{2}\rho_s R_s T_{\mathrm{trs}}, \tag{10}$$

$$E_{\mathrm{rot}} = \sum_{s=M}^{nm} \rho_s R_s T_{\mathrm{rot}}, \tag{11}$$

$$E_{\mathrm{vib}} = \sum_{s=M}^{nm} \frac{\rho_s R_s \Theta_{\mathrm{vib},s}}{\exp(\Theta_{\mathrm{vib},s}/T_{\mathrm{vib}}) - 1}, \tag{12}$$

$$E_{\mathrm{ele}} = \frac{3}{2}\rho_{\mathrm{ele}} R_{\mathrm{ele}} T_{\mathrm{ele}}. \tag{13}$$

The transport properties, including the viscosity, thermal conductivity, and binary diffusion coefficients for a gas mixture, are evaluated using Yos' formula [24], which is based on the first-order Chapman-Enskog approximation [25]. The collision cross sections are obtained using Gupta's method [26]. For e-N and e-O pairs, the collision cross section models developed by Fertig et al. [27, 28] were used. The diffusion coefficients are expressed using the formula developed by Curtiss and Hirschfelder [29]. Ambipolar diffusion is assumed for the charged species as $D_s^a = (1 + T_{\mathrm{ele}}/T_{\mathrm{trs}})\, D_s$, where D_s represents the effective diffusion coefficient of the ionic species. The electrical conductivity, σ, and electron component of the thermal conductivity, λ_{ele}, are evaluated based on the third-order Chapman-Enskog approximations [18, 19, 30] as.

$$\sigma = \frac{3e^2 n_{\mathrm{ele}}^2}{2kT_{\mathrm{ele}}} \sqrt{\frac{2\pi k T_{\mathrm{ele}}}{m_{\mathrm{ele}}}} \frac{\begin{vmatrix} q^{11} & q^{12} \\ q^{21} & q^{22} \end{vmatrix}}{\begin{vmatrix} q^{00} & q^{01} & q^{02} \\ q^{10} & q^{11} & q^{12} \\ q^{20} & q^{21} & q^{22} \end{vmatrix}}, \tag{14}$$

$$\lambda_{\mathrm{ele}} = \frac{75 n_{\mathrm{ele}}^2 k}{8} \sqrt{\frac{2\pi k T_{\mathrm{ele}}}{m_{\mathrm{ele}}}} \frac{q^{22}}{q^{11}q^{22} - (q^{12})^2}, \tag{15}$$

where the q elements are calculated using the number densities and collision cross sections. The collision cross sections used in the third-order approximation were obtained by Ghorui et al. [31] for collision pairs of electron and charged species, and by Laricchiuta et al. [32] for electron and neutral species.

For chemical reactions in high-temperature air, the gas is assumed to consist of 11 chemical species, i.e., N_2, O_2, NO, N_2^+, O_2^+, NO^+, N, O, N^+, O^+, and e^-, and 49 reactions are assumed to occur. The mass production rates, $\dot{w}_s$, are calculated using the forward and backward reaction rates of the chemical reactions. The chemical reactions considered herein are listed in Table 2. The forward reaction rate is calculated using an Arrhenius-type form as follows:

$$k_{\mathrm{f}}(T_{\mathrm{f}}) = C_r T_{\mathrm{f}}^{n_r} \exp\left(-\frac{\theta_r}{T_{\mathrm{f}}}\right). \tag{16}$$

The reaction-rate coefficients C_r, n_r, and θ_r are obtained from Park's work [33]. The backward reaction rate is obtained using the forward reaction rate and the equilibrium constant as

follows:

$$k_{\mathrm{b}}(T_{\mathrm{b}}) = \frac{k_{\mathrm{f}}(T_{\mathrm{b}})}{K^{\mathrm{eq}}(T_{\mathrm{b}})}. \tag{17}$$

The equilibrium constants for 48 chemical reactions (r=1–48 in Table 2) are calculated using the curve-fit formula and parameters obtained by Park's model [34]. For the only charge-exchange reaction between the molecular nitrogen and the ionized nitrogen (r=49 in Table 2), the curve-fit parameters are determined using Gupta's model [26].

The thermal nonequilibrium significantly affects the formation of an expansion flow in the nozzle as a result of rarefication, which is associated with supersonic expansion. The present analysis model introduces energy transfer between the internal energy modes: translation-rotation [35], translation-vibration [36, 37], translation-electron [38–40], rotation-vibration [41], rotation-electron [42, 43], and vibration-electron [44, 45]. In addition, the energy losses and releases for the vibrations and rotations associated with the chemical reactions reveal the dissociation energies for heavy particle-impact reactions. These are obtained using a non-preferential dissociation model [40]. The electron energy loss and release due to the electron-impact dissociation and ionization are also considered [17].

3.3 Turbulence Model

To reproduce the turbulent flow, the governing equations of the flow field are converted to Reynolds-averaged Navier-Stokes (RANS) equations using the Favre-averaging approach. A turbulence model is introduced to express the Reynolds stress derived in the average manner. In this paper, the shear stress transport turbulence model 2003 version (SST2003) [46] is adopted. Using the eddy viscosity, the transport properties in the flow-field equations are replaced as follows: (1) $\mu \to \mu + \mu_{\mathrm{t}}$, (2) $\lambda_{\mathrm{trs}} \to \lambda_{\mathrm{trs}} + \lambda_{\mathrm{t}}$, (3) $D_s \to D_s + D_{s,\mathrm{t}}$. In addition, the total energy is also replaced by $E \to E + \frac{3}{2}\rho k$, where k is the turbulent kinetic energy. The turbulent viscosity μ_{t} is obtained by solving two transport equations for the turbulent kinetic energy and specific dissipation rate in the SST model. The turbulent heat conductivity λ_{t} is evaluated using the turbulent viscosity, turbulent Prandtl number Pr_{t}, and specific heat at a constant pressure C_p, which is given by

$$\lambda_{\mathrm{t}} = \frac{\mu_{\mathrm{t}} C_p}{Pr_{\mathrm{t}}}. \tag{18}$$

Here, the turbulent Prandtl number Pr_{t} is set to 0.9. The turbulent diffusion coefficients $D_{s,\mathrm{t}}$ are calculated using the turbulent viscosity, turbulent Schmidt number Sc_{t}, total density ρ, and mass fraction C_s by

$$D_{s,\mathrm{t}} = \frac{\mu_{\mathrm{t}} C_s}{Sc_{\mathrm{t}} \rho}. \tag{19}$$

The turbulent Schmidt number Sc_{t}, which depends on the fluid and flow field, normally has a value between 0.5 and 1.

3.4 Radiation Model

The following two assumptions regarding the present radiation calculation are made: (1) The effects of scattering are negligible. (2) The radiation field is independent of time. By

Table 2: Chemical reactions.

r	Forward		Backward	C_r	n_r	θ_r	T_{f}	T_{b}
1–6	$N_2 + M_1$	$\rightleftharpoons$	$N + N + M_1$	7.0×10^{21}	-1.60	113,200	T_{f1}	T_{trs}
7–10	$N_2 + M_2$	$\rightleftharpoons$	$N + N + M_2$	3.0×10^{22}	-1.60	113,200	T_{f1}	T_{trs}
11	$N_2 + e^-$	$\rightleftharpoons$	$N + N + e^-$	1.2×10^{25}	-1.60	113,200	T_{ele}	T_{b1}
12–17	$O_2 + M_1$	$\rightleftharpoons$	$O + O + M_1$	2.0×10^{21}	-1.50	59,500	T_{f1}	T_{trs}
18–21	$O_2 + M_2$	$\rightleftharpoons$	$O + O + M_2$	1.0×10^{22}	-1.50	59,500	T_{f1}	T_{trs}
22–26	$NO + M_3$	$\rightleftharpoons$	$N + O + M_3$	5.0×10^{15}	0.00	75,500	T_{f1}	T_{trs}
27–31	$NO + M_4$	$\rightleftharpoons$	$N + O + M_4$	1.1×10^{17}	0.00	75,500	T_{f1}	T_{trs}
32	$NO + O$	$\rightleftharpoons$	$N + O_2$	8.4×10^{12}	0.00	19,450	T_{trs}	T_{trs}
33	$N_2 + O$	$\rightleftharpoons$	$NO + N$	6.4×10^{17}	-1.00	38,400	T_{trs}	T_{trs}
34	$N + N$	$\rightleftharpoons$	$N_2^+ + e^-$	4.4×10^{7}	1.50	67,500	T_{trs}	T_{trs}
35	$O + O$	$\rightleftharpoons$	$O_2^+ + e^-$	7.1×10^{2}	2.70	80,600	T_{trs}	T_{trs}
36	$N + O$	$\rightleftharpoons$	$NO^+ + e^-$	8.8×10^{8}	1.00	31,900	T_{trs}	T_{trs}
37	$N + e^-$	$\rightleftharpoons$	$N^+ + e^- + e^-$	2.5×10^{34}	-3.82	168,600	T_{ele}	T_{ele}
38	$O + e^-$	$\rightleftharpoons$	$O^+ + e^- + e^-$	3.9×10^{33}	-3.78	158,500	T_{ele}	T_{ele}
39	$NO^+ + O$	$\rightleftharpoons$	$N^+ + O_2$	1.0×10^{12}	0.50	77,200	T_{trs}	T_{trs}
40	$O_2^+ + N$	$\rightleftharpoons$	$N^+ + O_2$	8.7×10^{13}	0.14	28,600	T_{trs}	T_{trs}
41	$O^+ + NO$	$\rightleftharpoons$	$N^+ + O_2$	1.4×10^{5}	1.90	26,600	T_{trs}	T_{trs}
42	$O_2^+ + N_2$	$\rightleftharpoons$	$N_2^+ + O_2$	9.9×10^{12}	0.00	40,700	T_{trs}	T_{trs}
43	$O_2^+ + O$	$\rightleftharpoons$	$O^+ + O_2$	4.0×10^{12}	-0.09	18,000	T_{trs}	T_{trs}
44	$NO^+ + N$	$\rightleftharpoons$	$O^+ + N_2$	3.4×10^{13}	-1.08	12,800	T_{trs}	T_{trs}
45	$NO^+ + O_2$	$\rightleftharpoons$	$O_2^+ + NO$	2.4×10^{13}	0.41	32,600	T_{trs}	T_{trs}
46	$NO^+ + O$	$\rightleftharpoons$	$O_2^+ + N$	7.2×10^{12}	0.29	48,600	T_{trs}	T_{trs}
47	$O^+ + N_2$	$\rightleftharpoons$	$N_2^+ + O$	9.1×10^{11}	0.36	22,800	T_{trs}	T_{trs}
48	$NO^+ + N$	$\rightleftharpoons$	$N_2^+ + O$	7.2×10^{13}	0.00	35,500	T_{trs}	T_{trs}
49	$N_2 + N^+$	$\rightleftharpoons$	$N_2^+ + N$	1.0×10^{12}	0.50	12,200	T_{trs}	T_{trs}

$$
\begin{aligned}
M_1 &= \mathrm{N_2,\ O_2,\ NO,\ N_2^+,\ O_2^+,\ NO^+} \\
M_2 &= \mathrm{N,\ O,\ N^+,\ O^+} \\
M_3 &= \mathrm{N_2,\ O_2,\ N_2^+,\ O_2^+,\ NO^+} \\
M_4 &= \mathrm{NO,\ N,\ O,\ N^+,\ O^+}
\end{aligned}
$$

$$
\begin{aligned}
T_{\mathrm{f1}} &= \sqrt[3]{T_{\mathrm{trs}} T_{\mathrm{rot}} T_{\mathrm{vib}}} \\
T_{\mathrm{b1}} &= \sqrt{T_{\mathrm{trs}} T_{\mathrm{ele}}}
\end{aligned}
$$

considering a ray emitted from an infinitesimal element at a position to a point expressed in terms of the one-dimensional (1D) coordinate, s, the radiative transport equation is given by

$$\cos\theta \frac{dI_\lambda}{ds} = \kappa_\lambda (B_\lambda - I_\lambda), \tag{20}$$

where I_λ, κ_λ, and B_λ represent the intensity, absorption coefficient, and blackbody function at wavelength λ, respectively. The absorption coefficient includes the induced emission. Angle θ is defined as the angle between the ray and axis of the 1D coordinate s. The radiative heat flux emitted from the infinitesimal element is calculated over the entire solid angle and all wavelengths,

$$q^{\mathrm{rad}} = \iint I_\lambda \cos\theta d\Omega d\lambda. \tag{21}$$

The radiation term in Eqs. (3) and (7) are given with the radiative heat flux as follows:

$$S_{\mathrm{rad}} = \frac{\partial q_j^{\mathrm{rad}}}{\partial x_j}. \tag{22}$$

Because the radiation transport equation requires two integrations in the wavelength and spatial directions, its computational cost is too expensive to iteratively couple it with the flow-field simulation without any modeling. In this simulation, the radiation transport equation is modeled by calculating only in the radial direction of the cylindrical coordinate system [47]. In the present study, the three-band radiation model [12, 48] is used for wavelength integration. The wavelength-mean absorption coefficients and blackbody functions are evaluated *a priori* by classifying them into one of the three bands: Planck, Rosseland, and Gray-gas groups. The computational cost of the three-band radiation model is significantly lower than that of the line-by-line calculation, i.e., direct calculation.

3.5 Electric Field

The electric field equation is derived from Maxwell's equations and a generalized form of Ohm's law:

$$\nabla \cdot (\sigma \nabla \phi) = \nabla \cdot \left(\frac{\sigma}{e n_{\mathrm{e}}} \nabla p_{\mathrm{e}} \right). \tag{23}$$

The current-density vector is calculated using the electric potential and the electron pressure:

$$\mathbf{j} = \sigma \left(-\nabla \phi + \frac{\sigma}{e n_{\mathrm{e}}} \nabla p_{\mathrm{ele}} \right). \tag{24}$$

The electric field is defined as

$$\mathbf{E} = -\nabla \phi. \tag{25}$$

The Joule heating rate S_{joule} is thus given by

$$S_{\mathrm{joule}} = \mathbf{j} \cdot \mathbf{E}. \tag{26}$$

3.6 Numerical Implementation

The governing equations of the flow field are solved using a finite-volume formulation, and the equation system is transformed into the delta form. All the flow properties are set at the center of a control volume. Then, the advection fluxes in the N-S equations are calculated using the SLAU2 scheme [49] along with the MUSCL interpolation method for high accuracy. The viscous fluxes are evaluated using the second-order central difference method. Time integration is performed using an implicit time-marching method. For time integration, the lower-upper symmetric Gauss-Seidel (LU-SGS) method coupled with the point-implicit method is employed. Then, the electric-field equations are discretized using the finite-volume formulation, and the numerical fluxes are evaluated using the second-order central difference method. The GMRES method is used as the matrix solver for the electric-field equations, and sufficient convergence below a residual of 10^{-5} is achieved at each time step. These numerical models are implemented in "Arcflow/Arcwave" code.

3.7 Computational Conditions

In the L2K configuration, the diameters of the throat and nozzle exit are 29 mm and 100 mm, respectively. Figure 2 shows the computational domain of the L2K arc heater. A structured grid system is used for the present analysis. The number of computational grids is 311 (axial) $\times$ 75 (radial) points. The same computational domain and grid system are used for both flow-field and electric-field simulations, but their boundary conditions are different.

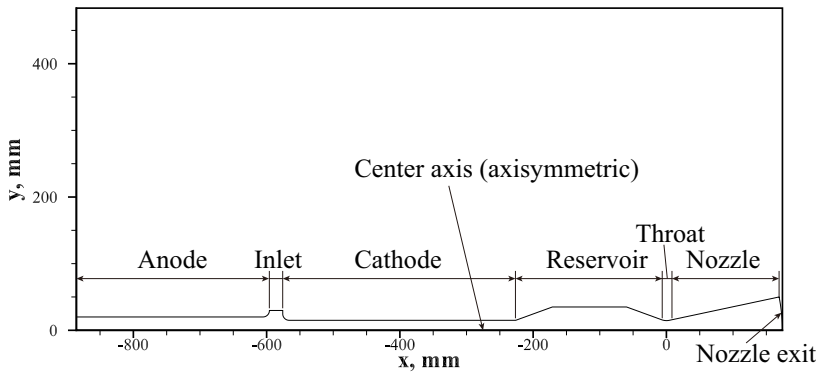

Figure 2: Computational domain for L2K arc-heated flow simulation.

For the flow-field simulation, the computational boundaries consist of the inflow boundary at the inlet, outflow boundary at the nozzle exit, axisymmetric boundary on the center axis, and wall boundaries on the electrode tubes, reservoir tube, throat section, and nozzle section. At the inflow boundary, the flow parameters are given using the mass flow rate, total temperature of the gas, and chemical components. The static pressure at the inflow boundary is extrapolated from an interior point. Because air is used as the test gas, the chemical components at the inflow are 0.765 of N_2 and 0.235 of O_2 in mass fractions. The nonslip condition for the velocity and no-pressure gradient normal to the wall are imposed at the wall boundary. At the walls, the translational, rotational, and vibrational temperatures are fixed at 1000 K. Because the present study neglects electrode sheaths, the electron temperature is assumed to be adiabatic at the wall. In addition, a noncatalytic (gradient free for the mass

fraction of chemical species) wall is assumed. At the outflow boundary, the gradient-free condition for all of the flow parameters is imposed.

For the electric-field simulation, no current is allowed to pass through the inlet, nozzle exit, or walls except for that in the electrodes. Axisymmetric conditions along the center axis are imposed, as well as the flow-field calculation. The following equipotential conditions are set on the electrodes: $V = 0$ on the cathode and $V = V_0$ on the anode. The arc voltage V_0 at the $(n+1)$th step is determined from the input current I, total current in the flow field I^n, and voltage at the V_0^n nth step, as follows:

$$V_0^{n+1} = V_0^n + \omega \left(\frac{I}{I^n} - 1 \right) V_0^n, \tag{27}$$

where ω is the relaxation parameter.

The input parameters are listed in Table 1. Because the configuration of L2K is large and this operation condition leads to a high-pressure state in the reservoir, the turbulence is expected to be enhanced in the heating section. Thus, to realize an accurate prediction, it is important to model and reproduce the effect of the turbulent flow. However, the value of the turbulent Schmidt number that significantly affects the turbulent diffusion is unclear for the arc-heated plasma flow situation. In this study, under the operating conditions, parametric studies for different cases were performed by setting the Schmidt numbers to 0.9, 0.7, and 0.5, along with the case involving no turbulent diffusion.

4 Results and Discussion

4.1 General Characteristics

The computational result of the arc-heated flow in L2K for the previously mentioned operation condition was obtained using the present analytical model. The turbulent Schmidt number was set to 0.7, but the basic flow structure was no different from that when using the other values. This section discusses the plasma flow characteristics for the case where Sc_{t}=0.7. To achieve a stable computation, a two-temperature model is used in the heating section ($x \leq 0$ m), while the four-temperature model is used in the nozzle section ($x > 0$ m). In this two-temperature model, the temperature is classified as the heavy-particle temperature (translational-rotational-vibrational temperature) and electron temperature. Because the pressure is sufficiently high and the flow field is close to the thermal equilibrium state in the heating section, the use of the two-temperature model is reasonable. This assumption is also used for the other cases.

Figures 3 and 4 show the distributions of the translational temperature and Mach number in the reservoir, throat, and nozzle sections of L2K. In addition, the distribution of the magnitude of current density in the heating section is shown in Fig. 5. In the heating section, the arc column near the center axis and the cold gas region are formed by the arc discharge. Because the arc discharge is attached to the end of the cathode (x=−225 mm), concentrating the electric current, it results in high Joule heating, and the test gas near the cathode end wall is heated. The high-temperature gas and cold gas were aggressively mixed in the reservoir section. In the heating section, the velocity is relatively low, and the flow is in a subsonic state. On the other hand, the arc-heated flow rapidly expands with a decrease in the translational temperature as a result of supersonic expansion in the nozzle section, after passing through the throat with choking. The maximum Mach number reaches approximately

4.3 at the nozzle exit. Because a thick boundary layer is formed near the nozzle wall, the effective cross-sectional area of the nozzle becomes small, which results in a decrease in the Mach number at the nozzle exit compared with values based on the consideration of the area ratios.

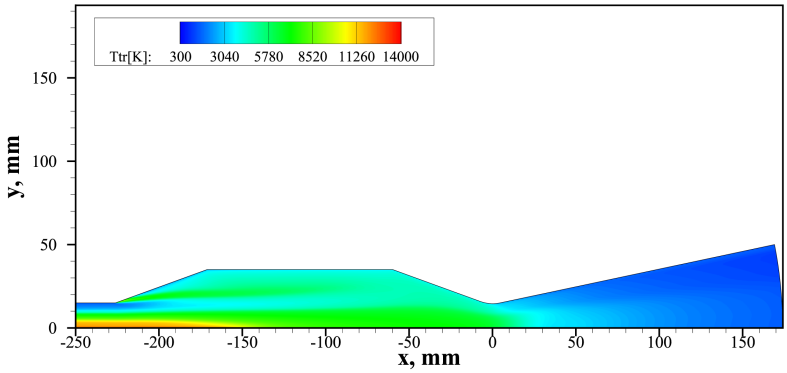

Figure 3: Distributions of translational temperature in reservoir, throat, and nozzle sections with turbulent diffusion model of Sc_{t}=0.7.

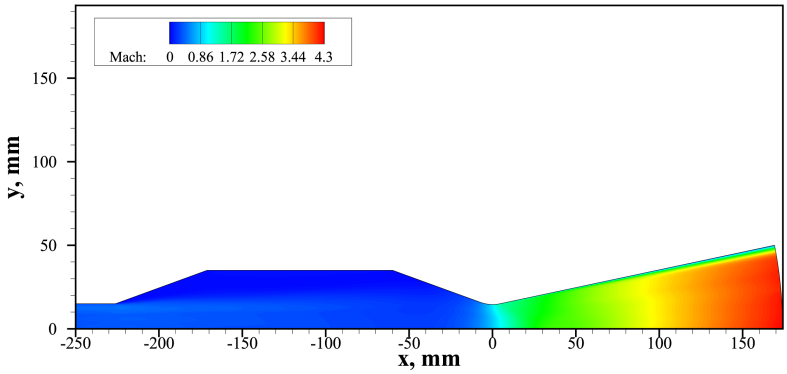

Figure 4: Distributions of Mach number in reservoir, throat, and nozzle sections with turbulent diffusion model of Sc_{t}=0.7.

Axial profiles of the species mole fractions and temperatures along the center axis in L2K are shown in Figs. 6(a) and 6(b), respectively. An arc column is formed in the heating section between the anode and cathode tubes. The dominant chemical species are atomic nitrogen and atomic oxygen in the heating section, which are caused by dissociation reactions. Electron and ion species are also generated by high Joule heating, and these charged species keep the arc discharge between the electrodes. The temperatures are almost in equilibrium, and the plasma flow is in local thermal equilibrium in the heating section. The temperature of the heavy particles is slightly higher than the electron temperature, and this is primarily because of the electron energy loss due to the electron-impact dissociation and ionization. In the present analysis model, from a viewpoint of computational cost, a relatively simple model for the electron energy losses by the reactions is used and effect of the electronically

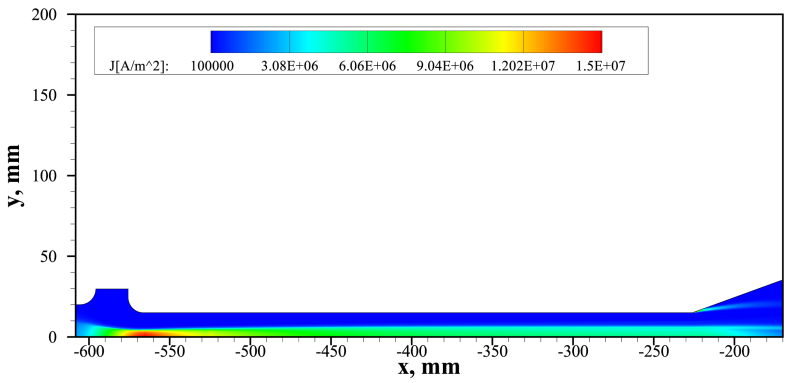

Figure 5: Distributions of current density in heating section with turbulent diffusion model of Sc_{t}=0.7.

metastable states of atoms and molecules is neglected. In addition, the radiation source term is considered in only the electron energy equation. However, as pointed out by Colonna et al. [50–52] and D'Ammando et al. [53], it is desired to introduce energy loss models considering metastable state and collisional-radiative process for more accurate prediction of arc discharge. More detailed discussion of this issue is left to future studies. In the reservoir, the charged species are rapidly reduced by recombination reactions as a result of a decrease in temperature. Instead, neutral species such as N, O, and N_2 become significant. In the nozzle section, molecular nitrogen appears as one of the dominant species as a result of recombination reactions. The temperatures rapidly decrease as a result of supersonic expansion after inflows into the throat, being separated in the nozzle.

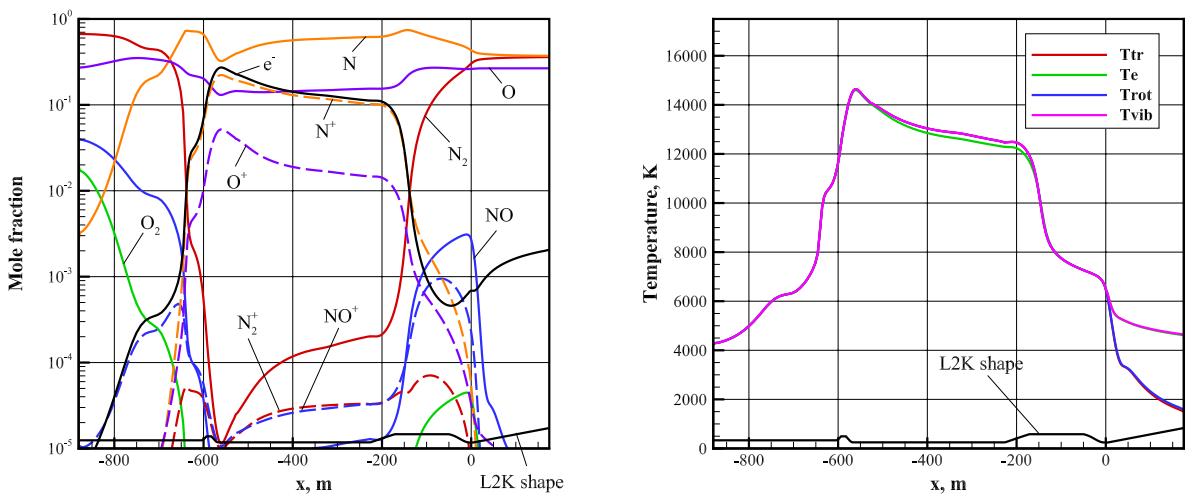

(a) Species mole fractions. (b) Temperature.

Figure 6: Axial profiles of species mole fractions and temperatures along center axis with turbulent diffusion model of Sc_{t}=0.7.

Enthalpy is an important parameter for arc-heated wind tunnels because a heating test and the reproduction of planetary entry are strongly affected by this value. In this paper,

the flow enthalpy is defined as the sum of the thermal, chemical, and kinetic energies per unit mass, and the pressure components, and is expressed by

$$h = e_{\mathrm{trs}} + e_{\mathrm{rot}} + e_{\mathrm{vib}} + e_{\mathrm{ele}} + \sum_{s}^{ns} C_s \Delta h_s^0 + \frac{1}{2} u_i u_i + \frac{p}{\rho}, \tag{28}$$

where the summation from the first term to the fourth in the right hand side of above equation is thermal component of the flow enthalpy. Moreover, the fifth, the sixth, and the seventh terms are chemical, kinetic, and pressure components, respectively. Figure 7 shows the axial profiles of the flow enthalpy along the center axis of L2K. The total enthalpy and each component of the enthalpy are illustrated in the figure. The total enthalpy becomes high between the electrode tubes from x=−600 to x=−200 mm because of the energy input caused by the arc discharge. A large part of the total enthalpy is the chemical component, followed by the thermal component. The energy derived by the arc discharge immediately adds to the chemical energy. In the reservoir section, the enthalpies at the center axis decrease with spatial diffusion in the radial direction, and they dissipate at the walls. The kinetic enthalpy is low in the reservoir, while it increases as a result of conversion from thermal energy to kinetic energy during the expansion in the nozzle.

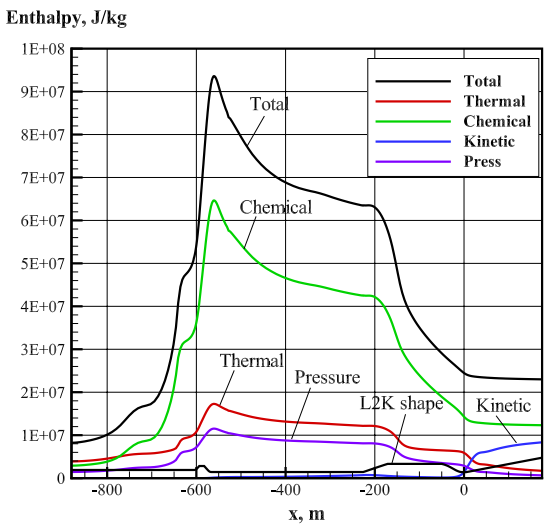

Figure 7: Axial profiles of flow enthalpy along center axis with turbulent diffusion model of Sc_{t}=0.7.

Figures 8(a) and 8(b) show radial profiles of the heat fluxes and translational temperature at the heating section at x=−300 mm and the reservoir section at x=−100 mm in L2K, respectively. The convective heat flux is obtained using the following expression:

$$q_j^{\mathrm{con}} = \lambda_{\mathrm{trs}} \frac{\partial T_{\mathrm{trs}}}{\partial x_j} + \lambda_{\mathrm{rot}} \frac{\partial T_{\mathrm{rot}}}{\partial x_j} + \lambda_{\mathrm{vib}} \frac{\partial T_{\mathrm{vib}}}{\partial x_j} + \lambda_{\mathrm{ele}} \frac{\partial T_{\mathrm{ele}}}{\partial x_j} + \rho \sum_{s}^{ns} h_s D_s \frac{\partial X_s}{\partial x_j}. \tag{29}$$

The total heat flux is defined as the sum of the convective heat flux, q_j^{con}, and radiative heat flux, q_j^{rad}. The radiation is generally rapidly enhanced when the electron temperature of a gas exceeds 10,000 K. In the heating section, it is found that the radiative and convective heat

fluxes are comparable because of the strong emission from the high-temperature region of the arc column. With a decrease in the temperature in the cold-gas region surrounding the arc column, the radiative heat flux decreases, while convective transfer plays a major role in the heat transfer between the column and cold gas. The radiation becomes low in the reservoir, because the peak temperature becomes lower than 8,000 K. Instead, the convective transfer becomes a dominant mechanism of heat transfer in the spatial direction. In particular, the turbulent component of the convection is large, and turbulence plays an important role in the reservoir section. It has been shown that arc-heated flows in L2K are strongly affected by radiation and turbulence transfers, as well as in other large-scale arc-heated wind tunnels such as the 750 kW JXWT and 20 MW AHF.

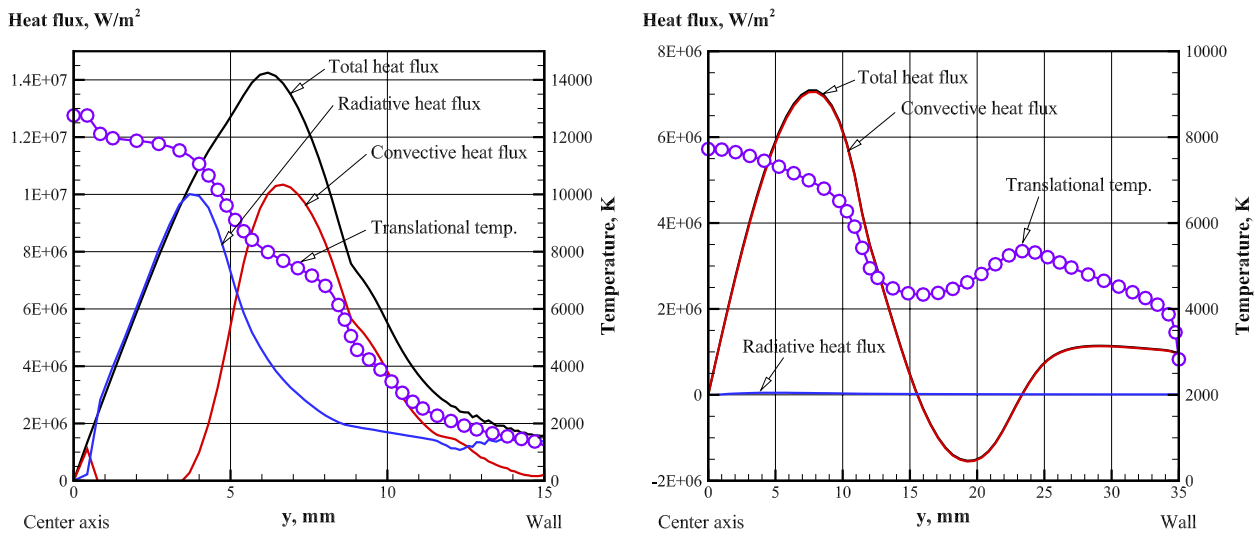

(a) Heating section (x=−300).

(b) Reservoir section (x=−100 mm).

Figure 8: Radial profiles of heat fluxes and translational temperatures with turbulent diffusion model of Sc_{t}=0.7.

Collision integrals for high temperature air species interactions by Gupta [26] and Fertig et al. [27, 28], which are widely used, are adopted in the present analysis model. However, these models are not necessarily updated. New collision integrals models for air species for predicting more accurate transport properties are developed [55–59]. Use of these recent models will be one of the future works in this study.

4.2 Grid Study

To investigate the computational grids independency in the present simulations, grid studies were performed for the cases without turbulent diffusion. We used fine computational grids with 476 (axial) × 100 (radial) points. The relative error in the total enthalpy at the center axis of the nozzle exit using the present and fine grids was within 2.2 %. This result indicates that the present computational grids are sufficiently converged.

4.3 Turbulent Diffusion

In L2K, turbulence is an important mechanism for the transfer of heat and the momentum of the arc-heated flow in the heating and reservoir sections. In particular, by performing several

numerical simulations, it was found that the effect of the turbulent diffusion on the species mass was high. Further, the turbulent Schmidt number directly affects the enhancement of the turbulent diffusion. This section presents the computational results obtained by changing the turbulent Schmidt number, and these are compared.

Table 3 lists comparisons of the arc voltages (V_0), reservoir pressure (p_r), and mass-averaged enthalpy (H_ave) at the nozzle exit for computation cases where the turbulent Schmidt numbers were varied between 0.9 and 0.5, and without turbulent diffusion, i.e., $Sc_\mathrm{t}\rightarrow\infty$. Here,

Table 3: Comparison of arc voltages.

Sc_t	V_0, V	p_r, Pa	H_ave, MJ/kg
–	819	1.19×10^5	12.3
0.9	808	1.18×10^5	12.5
0.7	787	1.18×10^5	12.1
0.5	699	1.14×10^5	11.1

the arc voltage is defined as the potential drop across the anode and cathode. The reservoir pressure is the pressure value at x=−100 mm on the center axis (y=0 mm) in the reservoir section. Note that the pressure is almost constant in the reservoir. The mass-averaged enthalpy is determined by the following expression:

$$H_\mathrm{ave} = \frac{\int \rho u h r dr}{\int \rho u r dr}, \tag{30}$$

where r is the radial coordinate.

The predicted arc voltages are between 819 and 699 V, while the measured voltage is approximately 720 V. It was confirmed that the arc voltage decreases with the turbulent Schmidt number. This means that the electrical energy input into the test gas decreases because the electrical current is maintained at a constant value. Charged species such as N^+ and e^- rapidly diffuse in spatial directions, particularly the radial direction, considering the turbulent diffusion model. This diffusion results in an increase in the electric conductivity of the arc column and a change in the arc-discharge formation in the heating section.

The pressures in the reservoir section show the tendency to slightly decrease with a decrease in the turbulent Schmidt number. The results show that the sensitivity of the pressure is low for the turbulent diffusion model. The present analysis model has the tendency to overestimate the energetic efficiency of the arc, and thus the pressure in the reservoir.

The mass-averaged enthalpy at the nozzle exit refers to the net energy input into the test gas by the arc discharge. As the turbulent Schmidt number and arc voltage decrease, the mass-averaged enthalpies also decrease. The mass-averaged enthalpy for the case of Sc_t=0.9 is slightly higher than that for the case without turbulent diffusion. This is related to the energy dissipation at the wall. The total heat flux profiles for cases with the turbulent diffusion model (Sc_t=0.9–0.5) and without turbulent diffusion on the walls are shown in Fig. 9. The peak total heat fluxes for all the cases appear on the end of the cathode and at the inlet of the reservoir (approximately x=−225 mm). This is because there is an arc discharge attached to this position and a high-temperature gradient in the normal direction to the wall.

A comparison of the computed results obtained using the turbulent diffusion models shows that the heat flux in the heating section decreases with the turbulent Schmidt number. In the heating section, the radiative heat flux is found to be an important component of the total heat flux because of the high-temperature gas in the arc column. A large decrease in the heat flux in the heating section is attributed to a decrease in the temperature in the arc column, which is caused by the arc voltage drop. Even though there are large discrepancies in the heat flux on the walls between the turbulent models, it is found that those of the mass-averaged enthalpy at the nozzle exit are small.

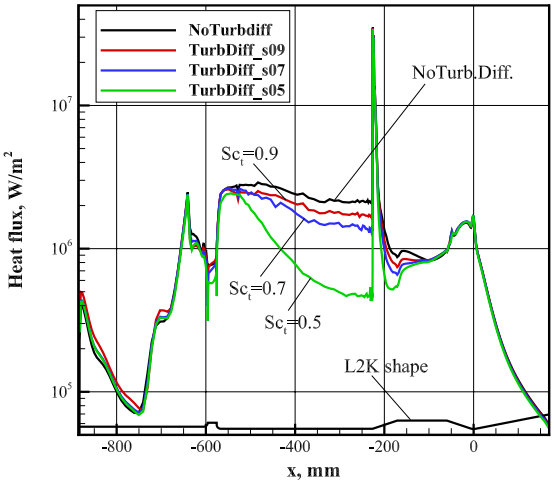

Figure 9: Comparison of total heat fluxes on walls with turbulent diffusion of turbulent Schmidt numbers between 0.9 and 0.5, and without turbulent diffusion.

Figure 10 shows a comparison of the radial profiles of the total enthalpy at the nozzle exit with turbulent diffusion using turbulent Schmidt numbers between 0.9 and 0.5, and without turbulent diffusion. Considering the turbulent diffusion model, the flow enthalpy becomes low near the center axis, and high in the outer region of the core flow. As a result, its distribution is close to uniform in the radial direction. Actually, the peak of the enthalpy at the core was not observed in the experiment. A primary component of the total enthalpy in the nozzle section is chemical. Thus, the flow enthalpy at the nozzle exit is significantly affected by the turbulent diffusion. In the present model, the circumferential momentum was not considered, and turbulence in that direction was neglected. However, it is possible that the turbulent diffusion model also involves the swirl effect produced by the magnetic field formed by the spin coil.

4.4 Comparison with Experiment

In the experiment, Pitot pressure profiles were obtained for the 50 mm flat-faced cylinder model exposed to the arc-heated flow in the test chamber of L2K. The measurement positions were x=50 mm and 100 mm downstream of the nozzle exit.

To reproduce a free jet nozzle flow in the test chamber using numerical analysis, simulations of the flow field around the test model were performed. The analytical models were

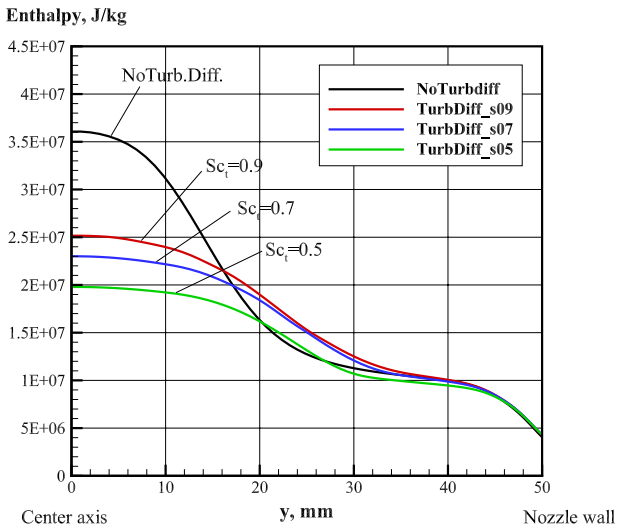

Figure 10: Comparison of radial profile of flow enthalpy at nozzle exit with turbulent diffusion using turbulent Schmidt numbers between 0.9 and 0.5, and without turbulent diffusion.

basically the same as those used in the arc-heated flow simulation in L2K, as previously mentioned, and the "Arcflow/Arcwave" code was used. The electrical field, radiation field, and turbulent flow were not considered because these effects were expected to be low in the test chamber. The AUSM-DV scheme [54] was selected as the advection scheme for the flow-field equations.

Figure 11 illustrates the computational domain and boundaries for the simulations of the nozzle flow around the test model. The number of grids was 300 (axial) $\times$ 190 (radial) points. At the inflow boundary, the flow parameters were given by the computational results of the L2K arc-heated flow at the nozzle exit. The nonslip, no-pressure gradient normal to the wall and noncatalytic conditions were imposed at the wall boundary. The wall temperature was set to 300 K. Under ambient conditions, a static pressure of 10 Pa and temperature of 300 K were imposed. In addition, the mass fractions under the ambient conditions were the same as those of the air. At the outflow boundary, the gradient-free condition was imposed for all the flow parameters. In the present numerical simulations, four cases that gave the computed results of arc-heated flows in L2K with the turbulent Schmidt numbers of 0.9, 0.7, and 0.5, and without turbulent diffusion were considered.

For comparison with Pitot pressure measurements, the frozen stagnation pressure can be determined based on the simulation results for the nozzle flow, as in the following procedure. First, the pressure and temperature jumps across the normal shock are evaluated by

$$p_{21} = \begin{cases} 1 + \dfrac{2\gamma}{\gamma+1}\left(M^2 - 1\right), & (M > 1) \\ 1, & (otherwise) \end{cases} \tag{31}$$

$$T_{21} = \begin{cases} p_{21}\dfrac{(\gamma-1)\,p_{21} + (\gamma+1)}{(\gamma+1)\,p_{21} + (\gamma-1)}, & (M > 1) \\ 1, & (otherwise) \end{cases} \tag{32}$$

where γ and M are the frozen specific heat ratio and Mach number, respectively, which are obtained from the simulation results. Then, the pressure increase from the post-shock layer

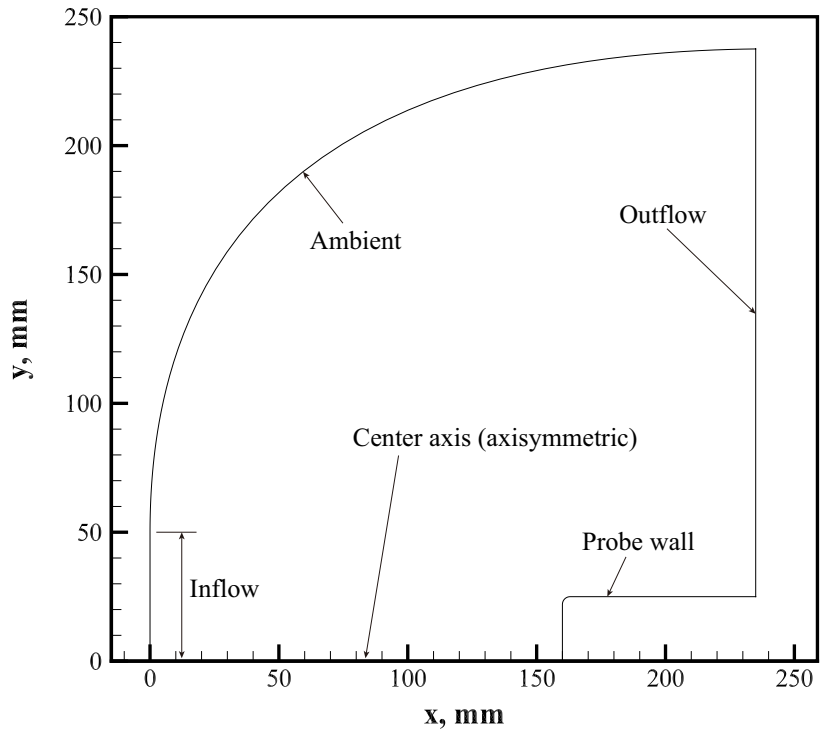

Figure 11: Computational domain and boundary conditions for L2K nozzle flow around test model in test chamber.

to stagnation is calculated by

$$p_{02} = \left(\frac{1 + \frac{\gamma - 1}{2} M^2}{T_{21}} \right)^{\frac{\gamma}{\gamma - 1}} . \tag{33}$$

Finally, the frozen stagnation pressure is given by

$$p_0 = p \cdot p_{21} \cdot p_{02}. \tag{34}$$

Figure 12 shows the distribution of the frozen stagnation pressure around the 50 mm flat-faced test model in the L2K test chamber. For the boundary condition at the inflow boundary, the computational result of the arc-heated flow in L2K obtained with the turbulent diffusion model of Sc_{t}=0.7 is used. The two white lines in this figure are the measurement points for the Pitot pressure in the experiment.

A comparison of the Pitot pressures obtained in the experiment and simulation is shown in Fig. 13. From the measured Pitot pressure, it is confirmed that the core flows at x=50 and 100 mm have ranges of y=−40∼40 mm and y=−35∼35 mm, respectively. In addition, the Pitot pressures have peaks near the edges of the core (approximately y = 38 mm and y = 32 mm), while the pressures slightly decrease near the center axis. The computed frozen stagnation pressures for all the cases overestimate the experimental results. This is mainly because

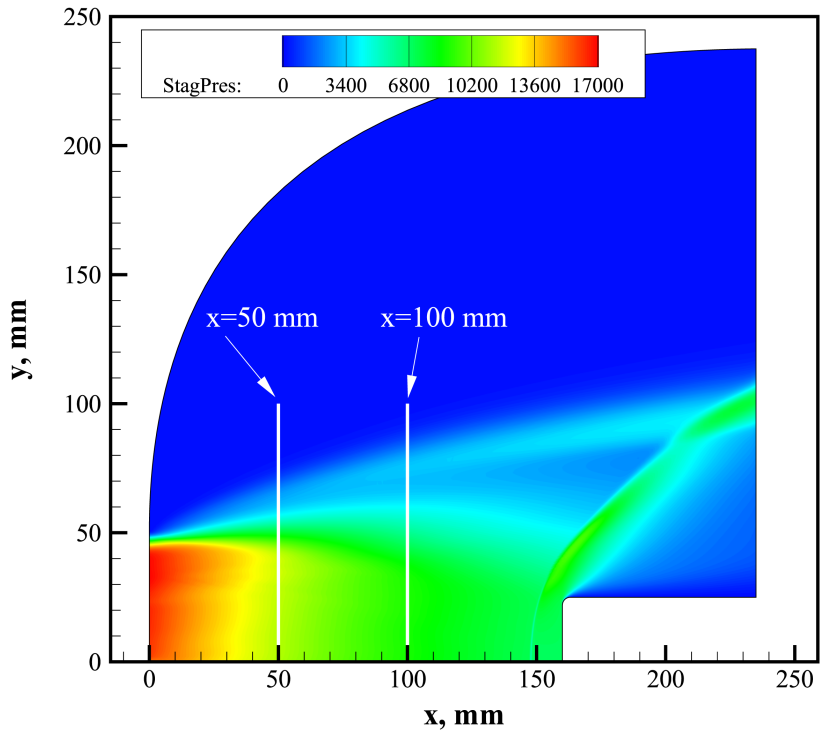

Figure 12: Distribution of frozen stagnation pressure around test model in L2K test chamber for case using turbulent diffusion model of Sc_{t}=0.7.

the chamber pressures are over-predicted, as mentioned earlier. Discrepancies between the results of the experiment and simulation are improved by decreasing the turbulent Schmidt number, i.e., enhancing the turbulent diffusion. In particular, the coordinate of the peak frozen stagnation pressure moves toward the outer side. Turbulent diffusion results in a smoothing of the pressure distribution in the radial direction at the nozzle exit as well as the flow enthalpy. The results show that the turbulent diffusion model for mass species is important for large-scale arc heater prediction.

In this study, the RANS model was used as the turbulence model, and was generally tuned so that the model could appropriately reproduce a specific flow field. Thus, the prediction performances for all the plasma flow simulations were not necessarily good. With respect to the turbulent Schmidt number, the situation was the same. In the present study, it was shown that varying the turbulent Schmidt number from 0.7 to 0.5 was likely to be optimum for L2K simulations. However, for the other arc-heated wind tunnels, this value is not necessarily effective at reproducing a plasma flow field. It is possible that tuning the turbulent diffusion model or using a large-eddy simulation approach will be required.

Four-temperature approach is used in prediction of the L2K arc-heated flow in the nozzle and test chamber. However, it was pointed out by Colonna et al. [60–62] that this model is not adequate for modeling expansion. Recently, expansion process in a nozzle has been investigated in detail using the state-to-state approach. These models can contribute to improve prediction performance of the arc-heated flow.

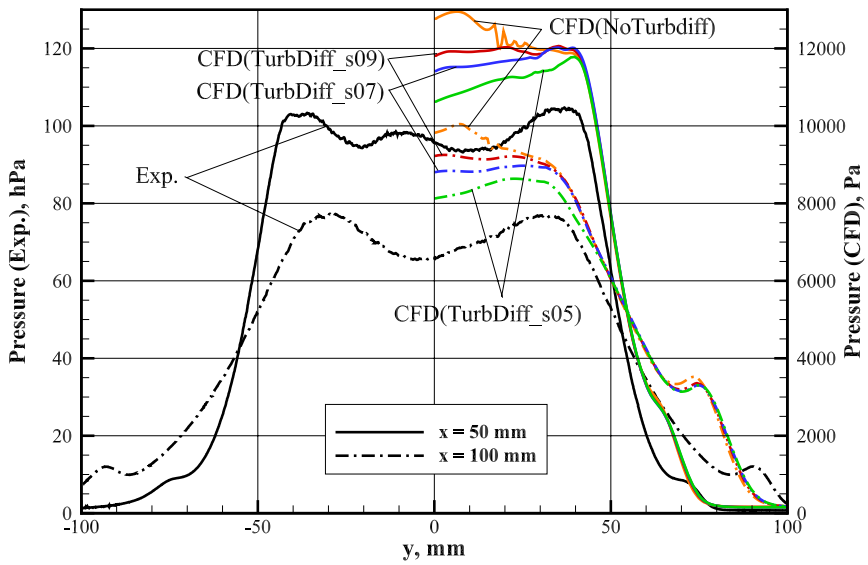

Figure 13: Comparison of Pitot pressures measured in experiment and frozen stagnation pressures by simulation result.

5 Conclusions

In this study, an analytical model was constructed for the arc-heated flow in L2K in the German Aerospace Center (DLR; Deutsches Zentrum für Luft- und Raumfahrt), which is one of the most commonly used Huels-type arc-heated wind tunnels. The thermochemical nonequilibrium, discharge behavior, radiation, and turbulence models were incorporated in the present model. In addition, a higher-order approximation model of the transport properties was introduced. Numerical simulations using the present analytical model were performed for cases with turbulent diffusion using several turbulent Schmidt numbers and without the turbulent diffusion effect for species mass.

The fundamental characteristics of the arc-heated flow in L2K were obtained by performing computations. The arc discharge in the heating section and supersonic expansion in the nozzle section in L2K were reproduced. The flow enthalpy components were investigated in L2K, and the cascade process from electrical energy to kinetic energy by the arc discharge was discussed. It was confirmed that radiation and turbulence are significant mechanisms in the transfer of heat from an arc column to the outer cold gas.

By performing parametric studies involving varying the turbulent Schmidt number from 0.9 to 0.5, the effects of turbulent diffusion on the species mass were investigated. It was found that turbulent diffusion significantly affects the heat dissipation on the wall in the heating section and enthalpy distribution at the nozzle exit. However, the chamber pressure and net energy of the gas at the nozzle exit were relatively insensitive to the turbulence Schmidt numbers. Pitot pressure profiles measured in the test chamber in L2K were compared with the results obtained from the present numerical simulation based on a frozen stagnation pressure theory. The predicted pressure profiles were improved when the turbulent diffusion for the species mass was enhanced. The results showed that modeling the turbulent diffusion is important for large-scale arc-heated wind tunnels.

In practice, arc discharge is an unsteady process at high frequencies, and the impact of arc rotation on the heating is not well known. The results obtained in the present study showed that the analytical model still overestimates the electrical efficiency of the arc and pressure. The reasons may include a negligible circumferential momentum and swirl effect, and radiation in the axial direction, in addition to the complicated arc discharge behavior. Additional efforts are required to appropriately model these effects to realize further improvement in the reproduction of actual arc-heated flows, which can be performed using simulations supported by dedicated measurements with advanced diagnostics. However, it was also concluded that there has been good progress because of the identification of the turbulent diffusion.

Acknowledgments

The authors would like to thank Dr. Minghao Yu (Xi'an University of Technology, China) for the helpful discussions regarding the present transport property model. This work was supported by JSPS KAKENHI Grant Number 17K14871. The computations were performed using the computational facilities (HITACHI HA8000-tc/HT210 and FUJITSU PRIMERGY CX400) at the Research Institute for Information Technology, Kyushu University.

References

[1] Y. Watanabe, K. Ishida, and H. Shirai. "Spectroscopic Analysis of NO Band Emissions from Arc-Heated Air Flows in a 750 kW Arc-Heated Wind Tunnel". NAL TR-1417, National Aerospace Laboratory, Chofu, Japan, 2000.

[2] H. Takayanagi, M. Mizuno, K. Fujii, T. Suzuki, and K. Fujita. "Arc Heated Wind Tunnel Flow Diagnostics using Laser-Induced Fluorescence of Atomic Species". *AIAA Paper 2009-1449*, 2009.

[3] H. Takayanagi, M. Mizuno, K. Fujii, T. Suzuki, and K. Fujita. "Arc Wind Tunnel Flow Characterization Measured by Laser-Induced Fluorescence of Atomic Species". *AIAA Paper 2009-4241*, 2009.

[4] J.H. Grinstead, D.M. Diver, and G.A. Raiche. "Radial Profiles of Arcjet Flow Properties Measured with Laser-Induced Fluorescence of Atomic Nitrogen". *AIAA Paper 2003-400*, 2003.

[5] M. Mizuno, K. Ishida, T. Matsuzaki, T. Ito, and Y. Watanabe. "Spectral and Heating Characteristics in the Arc Column of the 0.75 MW Arc-Heated Wind Tunnel". In *Proceedings of 23th International Symposium on Space Technology and Science*, ISTS 2002-e-4, Matsue, Shimane, Japan, May 26 - June 2 2002.

[6] Y. Takahashi, T. Abe, H. Takayanagi, M. Mizuno, H. Kihara, and K. Abe. "Nonequilibrium Plasma Flow Properties in Arc-Heated Wind Tunnels". *AIAA Paper 2012-1240*, 2012.

[7] M.W. Winter, D.K. Prabhu, G.A. Raiche, I. Terrazas-Salinas, and F.C.L. Hui. "Emission Spectroscopic Measurement with an Optical Probe in the NASA Ames IHF Arc Jet Facility". *AIAA Paper 2012-1016*, 2012.

[8] K. Abe, T. Kameyama, H. Kihara, M. Nishida, K. Ito, and H. Tanno. "Computation and Experiment of Nonequilibrium Nozzle Flow of Arc-heated Air". *Journal of Thermophysics and Heat Transfer*, 19(4):428–434, 2005.

[9] G. Colonna and M. Capitelli. "Boltzmann and Master Equations for Magnetohydrodynamics in Weakly Ionized Gases". *Journal of Thermophysics and Heat Transfer*, 22(3):414–423, July-Sept. 2008.

[10] T. Sakai, K. Sawada, and M. Mitsuda. "Application of Planck-Rosseland-Gray Model for High-Enthalpy Arc Heaters". *Journal of Thermophysics and Heat Transfer*, 15(2):176–183, April-June 2001.

[11] J.P. Lee, C. Kim, and K.H. Kim. "Accurate Computations of Arc-Heater Flows Using Two-Equation Turbulence Models". *Journal of Thermophysics and Heat Transfer*, 21(1):67–76, Jan.-Mar. 2007.

[12] T. Sakai. "Computational Simulation of High-Enthalpy Arc Heater Flows". *Journal of Thermophysics and Heat Transfer*, 21(1):77–85, Jan.-Mar. 2007.

[13] Y. Takahashi, H. Kihara, and K. Abe. "Numerical Investigation of Nonequilibrium Plasma Flows in Constrictor- and Segmented-Type Arc Heaters". *Journal of Thermophysics and Heat Transfer*, 24(1):31–39, 2010.

[14] Y. Takahashi, H. Kihara, and K. Abe. "The Effects of Radiative Heat Transfer in Arc-Heated Nonequilibrium Flow Simulation". *Journal of Physics D: Applied Physics*, 43(18):185201, 2010.

[15] T. Matsuzaki, K. Ishida, Y. Watanabe, K. Miho, H. Itagaki, and T. Yoshinaka. "Constructions and Characteristics of the 750 kW Arc Heated Wind Tunnel". NAL TM-760, National Aerospace Laboratory, Chofu, Japan, 2001.

[16] T.M. Hightower, J.A. Balboni, C.L.M. Donald, K.F. Anderson, and E.R. Martinez. "Enthalpy by Energy Balance for Aerodynamic Heating Facility at NASA Ames Research Center Arc Jet Complex". In *Proceedings of the 48th International Instrumentation Symposium*, ISA TP02-AERO-2000, Instrumentation, Systems, and Automation Society, San Diego, CA, USA, 2002.

[17] Y. Takahashi, H. Kihara, and K. Abe. "Turbulence and Radiation Behaviours in Large-Scale Arc Heaters". *Journal of Physics D: Applied Physics*, 44(8):085203, 2011.

[18] H. Katsurayama and T. Abe. "Thermochemical Nonequilibrium Modeling of a Low-Power Argon Arcjet Wind Tunnel". *Journal of Applied Physics*, 113:053304, 2013.

[19] M. Yu, K. Yamada, Y. Takahashi, k Liu, and T. Zhao. "Flow-Field Differences and Electromagnetic-Field Properties of Air and N2 Inductively Coupled Plasmas". *Physics of Plasmas*, 23(12):123523, 2016.

[20] A. Sahai, N.N. Mansour, B. Lopez, and M. Panesi. "Modeling of High Pressure Arc-Discharge with a Fully-Implicit Navier–Stokes Stabilized Finite Element Flow Solver". *Plasma Sources Science and Technology*, 26(5):055012, 2017.

[21] A. Gülhan, B. Esser, and U. Koch. "Experimental Investigation of Reentry Vehicle Aerothermodynamic Problems in Arc-Heated Facilities". *Journal of Spacecraft and Rockets*, 38(2):199–206, 2001.

[22] L. Steffens, U. Koch, B. Esser, and A. Gülhan. "Characterization of weakly ionized argon flows for radio blackout mitigation experiments". In *Progress in Flight Physics–Volume 9*, volume 9, pages 335–348. EDP Sciences, 2017.

[23] A. Gülhan. "Advanced ablation characterization and modelling". In *8th European Workshop on Thermal Protection Systems and Hot Structures*, Noordwijk, The Netherlands, April 19 - 22 2016.

[24] J.M. Yos. "Transport Properties of Nitrogen, Hydrogen Oxygen and Air to 30,000 K". *TRAD-TM-63-7,* Research and Advanced Development Division, AVCO Corp., 1963.

[25] J.O. Hirschfelder, C.F. Curtiss, and R.B. Bird. *Molecular Theory of Gases and Liquids.* Wiley, New York, 1954.

[26] R.N. Gupta, J.M. Yos, R.A. Thompson, and K.P. Lee. "A Review of Reaction Rates and Thermodynamic and Transport Properties for an 11-Species Air Model for Chemical and Thermal Nonequilibrium Calculations to 30000 K". *NASA RP-1232*, Aug. 1990.

[27] M. Fertig, A. Dohr, and H.H. Frühaufu. "Transport Coefficients for High-Temperature Nonequilibrium Air Flows". *AIAA Paper 98-2937*, 1998.

[28] M. Fertig, A. Dohr, and H.H. Frühauf. "Transport Coefficients for High-Temperature Nonequilibrium Air Flows". *Journal of Thermophysics and Heat Transfer*, 15(2):148–156, April-June 2001.

[29] C.F. Curtiss and J.O. Hirschfelder. "Transport Properties of Multicomponent Gas Mixture". *Journal of Chemical Physics*, 17(6):550–555, June 1949.

[30] R.S. Devoto. "Simplified Expressions for the Transport Properties of Ionized Monatomic Gases". *Physics of Fluid*, 10(10):2105–2112, 1967.

[31] S. Ghorui and A.K. Das. "Collision integrals for charged-charged interaction in two-temperature non-equilibrium plasma". *Physics of Plasmas*, 20(9):093504, 2013.

[32] A. Laricchiuta, D. Bruno, M. Capitelli, C. Catalfamo, R. Celiberto, G. Colonna, P. Diomede, D. Giordano, C. Gorse, S. Longo, D. Pagano, and F. Pirani. "High temperature Mars atmosphere. Part I: transport cross sections". *The European Physical Journal D*, 54:607–612, 2009.

[33] C. Park. "Assessment of a Two-Temperature Kinetic Model for Dissociating and Weakly Ionizing Nitrogen". *Journal of Thermophysics and Heat Transfer*, 2(1):8–16, Jan.-March 1988.

[34] C. Park. *Nonequilibrium Hypersonic Aerothermodynamics.* Wiley, New York, 1990.

[35] J.G. Parker. "Rotational and Vibrational Relaxation in Diatomic Gases". *The Physics of Fluids*, 2(4):449–462, July-Aug. 1959.

[36] R.C. Millikan and D.R. White. "Systematics of Vibrational Relaxation". *The Journal of Chemical Physics*, 39(12):3209–3213, Dec. 1963.

[37] C. Park. "Problems of Rate Chemistry in the Flight Regimes of Aeroassisted Orbital Transfer Vehicles". *AIAA Paper 84-1730*, 1984.

[38] J.P. Appleton and K.N.C. Bray. "The Conservation Equations for a Nonequilibrium Plasma". *Journal of Fluid Mechanics*, 20(4):659–672, June 1964.

[39] M. Mitchner and C.H. Kruger Jr. *Partially Ionized Gases*. Wiley, New York, 1973.

[40] P.A. Gnoffo, R.N. Gupta, and J.L. Shinn. "Conservation Equations and Physical Models for Hypersonic Air Flows in Thermal and Chemical Nonequilibrium". *NASA TP-2867*, Feb. 1989.

[41] C. Park. "Rotational Relaxation of N_2 Behind a Strong Shock Wave". *Journal of Thermophysics and Heat Transfer*, 18(4):527–533, Oct.-Dec. 2004.

[42] M. Nishida and M. Matsumoto. "Thermochemical Nonequilibrium in Rapidly Expanding Flows of High-Temperature Air". *Zeitschrift für Naturforschung, Teil A: Physik, Physikalische Chemie, Kosmophysik*, 52(4):358–368, 1997.

[43] S.S. Lazdinis and S.L. Petrie. "Free Electron and Vibrational Temperature Nonequilibrium in High Temperature Nitrogen". *Physics of Fluids*, 17(8):1539–1546, Aug. 1974.

[44] J.H. Lee. "Electron-Impact Vibrational Relaxation in High-Temperature Nitrogen". *Journal of Thermophysics and Heat Transfer*, 7(3):399–405, July-Sept. 1993.

[45] C. Park and S.H. Lee. "Validation of Multitemperature Nozzle Flow Code". *Journal of Thermophysics and Heat Transfer*, 9(1):9–16, Jan.-Mar. 1995.

[46] F.R. Menter, M. Kuntz, and R. Langtry. "Ten Years of Industrial Experience with the SST Turbulence Mode". *Turbulence, Heat and Mass Transfer 4, ed: K. Hanjalic, Y. Nagano, and M. Tummers, Begell House, Inc.*, pages 625–632, 2003.

[47] A.S. Kesten. "Radiant Heat Flux Distribution in a Cylindrically-Symmetric Nonisothermal Gas with Temperature-Dependent Absorption Coefficient". *J. Quant. Spectrosc. Radiat. Transfer*, 8:419–434, 1968.

[48] T. Sakai and J. Olejniczak. "Improvements in a Navier-Stokes Code for Arc Heater Flows". *AIAA Paper 2003-3782*, 2003.

[49] K. Kitamura and E. Shima. "Towards shock-stable and accurate hypersonic heating computations: A new pressure flux for AUSM-family schemes". *Journal of Computational Physics*, 245:62–83, 2013.

[50] G. Colonna, L. Pietanza, and G. D'Ammando. "Self-consistent collisional-radiative model for hydrogen atoms: Atomatom interaction and radiation transport". *Chemical Physics*, 398(Supplement C):37 – 45, 2012. Chemical Physics of Low-Temperature Plasmas (in honour of Prof Mario Capitelli).

[51] G. Colonna, G. D'Ammando, L. Pietanza, and M. Capitelli. "Excited-state kinetics and radiation transport in low-temperature plasmas". *Plasma Physics and Controlled Fusion*, 57(1):014009, 2014.

[52] G. Colonna, G. D'Ammando, and L. Pietanza. "The role of molecular vibration in nanosecond repetitively pulsed discharges and in DBDs in hydrogen plasmas". *Plasma Sources Science and Technology*, 25(5):054001, 2016.

[53] G. D'Ammando, M. Capitelli, F. Esposito, A. Laricchiuta, L.D. Pietanza, and G. Colonna. "The role of radiative reabsorption on the electron energy distribution functions in H2/He plasma expansion through a tapered nozzle". *Physics of Plasmas*, 21(9):093508, 2014.

[54] Y. Wada and M.S. Liou. "A Flux Splitting Scheme with High-Resolution and Robustness for Discontinuities". *AIAA Paper 94-0083*, 1994.

[55] A. Murphy. "Transport coefficients of air, argon-air, nitrogen-air, and oxygen-air plasmas". *Plasma Chemistry and Plasma Processing*, 15(2):279–307, 1995.

[56] M.J. Wright, D. Bose, G.E. Palmer, and E. Levin. "Recommended collision integrals for transport property computations, Part 1: Air species". *AIAA journal*, 43(12):2558, 2005.

[57] M. Capitelli, G. Colonna, C. Gorse, and A. D'Angola. "Transport Properties of High Temperature Air in Local Thermodynamic Equilibrium". *The European Physical Journal D*, 11:279–289, 2000.

[58] A. D'Angola, G. Colonna, A. Bonomo, D. Bruno, A. Laricchiuta, and M. Capitelli. "A phenomenological approach for the transport properties of air plasmas". *The European Physical Journal D-Atomic, Molecular, Optical and Plasma Physics*, 66(8):1–6, 2012.

[59] B. Sourd, J. Aubreton, M.F. Elchinger, M. Labrot, and U. Michon. "High temperature transport coefficients in e/C/H/N/O mixtures". *Journal of Physics D: Applied Physics*, 39(6):1105, 2006.

[60] G. Colonna and M. Capitelli. "Self-Consistent Model of Chemical, Vibrational, Electron Kinetics in Nozzle Expansion". *Journal of Thermophysics and Heat Transfer*, 15(3):308–316, July-Sept. 2001.

[61] G. Colonna, M. Tuttafesta, M. Capitelli, and D. Giordano. "Non-Arrhenius NO Formation Rate in One-Dimensional Nozzle Air ow". *Journal of thermophysics and heat transfer*, 13(3), 1999.

[62] G. Colonna, L.D. Pietanza, and M. Capitelli. "Recombination-Assisted Nitrogen Dissociation Rates Under Nonequilibrium Conditions". *Journal of Thermophysics and Heat Transfer*, 22(3):399–406, July-Sept. 2008.